Ultramicroscopy 285 (2026) 114408

Contents lists available at ScienceDirect

Ultramicroscopy

journal homepage: www.elsevier.com/locate/ultramic

Brightness optimization in a 200 keV DTEM source by geometry-driven aberration suppression

Paul Denham [a,*], Pietro Musumeci [a], Daniel J. Masiel [b], Bryan W. Reed [b]

[a] Department of Physics and Astronomy, University of California, Los Angeles, CA, USA
[b] Integrated Dynamic Electron Solutions (IDES, Inc.), Pleasanton, CA, USA

ARTICLE INFO

Keywords:
Dynamic transmission electron microscopy (DTEM)
Ultrafast electron microscopy (UTEM)
Electrostatic lenses
Electron source aberrations
Electron source brightness optimization
Space charge

ABSTRACT

High temporal resolution dynamic transmission electron microscopy (DTEM) requires substantially higher peak currents than conventional TEM sources can sustain without severe brightness loss, motivating a redesign of the electron gun. This work targets improving the brightness in a 200 keV electrostatic electron gun for DTEM by mitigating aberrations through optimizing conductor geometry. The cathode–anode assembly is reconfigured to act simultaneously as an accelerator and condenser pre-lens, confining the beam size in regions of strong field curvature. A third-order off-axis transfer map with Green's-function evaluation of image errors, validated against Superfish and GPT, quantifies how space-charge-driven divergence growth couples into spherical aberration and guides voltage/geometry choices. Along a minimum-spot operating contour, the spherical aberration coefficient is reduced from > 150 mm to ∼5–10 mm at 200 keV while preserving a ≤ 10 μm exit-aperture spot for MTE = 0.1–1 eV and ∼1 mA peak current. The results establish geometry-driven gun redesign as a practical route to higher-brightness, low-aberration electron sources for next-generation time-resolved microscopy.

1. Introduction

Ultrafast and dynamic transmission electron microscopy (UTEM and DTEM) extend conventional TEM into the time domain, enabling direct imaging of structural dynamics on femtosecond to nanosecond scales. Foundational work in ultrafast electron diffraction and microscopy established the framework for capturing structural changes with high temporal resolution [1–5]. UTEM implementations typically use stroboscopic pump–probe schemes in which many identical pump events are averaged, whereas DTEM operates in a true single-shot mode using a single, high-charge electron pulse. By adding the temporal dimension to imaging with nanometer-scale spatial resolution, these instruments hold the potential for direct observation of transient processes such as phase transitions, defect motion, and nanoscale excitations.

A central requirement for DTEM is delivering sufficient electron dose in a single exposure, particularly when imaging irreversible or radiation-sensitive systems. Meeting this requirement within nanosecond or shorter pulse durations requires peak currents in the milliampere range far beyond those attainable with thermionic or field-emission guns, making laser-driven photoemission the only practical route to reach the necessary charge per pulse. The normalized emittance of a uniformly illuminated photocathode remains essentially constant, if the emitted charge is kept below the space-charge saturation limit [6–8], but the transverse angular spread increases with current. Injected into an electrostatic gun, these larger initial angles sample stronger on-axis field curvature, resulting in third-order trajectory errors dominated by spherical aberration. The outcome is a rapid loss of usable phase space and brightness at the current levels required for single-shot imaging [9,10].

Work at multiple research facilities has validated the feasibility of 200 keV dynamic transmission electron microscopy as a powerful tool for time-resolved materials investigations [11–15]. These systems highlighted the fundamental trade-off between achieving milliampere peak currents and maintaining resolution, with spherical aberration coefficients typically in the tens to hundreds of millimeters.

Several approaches have been explored to mitigate this trade-off, including low-emittance photocathodes [16] and external multipole aberration correctors [17,18]. However, for high-current electrostatic guns, the values of the spherical aberration coefficient C_s remain well above what is required to achieve an ultrasmall focus at the specimen plane. Typically, one clips the unusable portion of the source phase space but if the goal is to retain the full emitted current without any particle losses, a redesigned gun geometry might offer a more attractive pathway to suppress the resulting aberrations.

* Corresponding author.
E-mail address: pdenham@physics.ucla.edu (P. Denham).

https://doi.org/10.1016/j.ultramic.2026.114408
Received 26 November 2025; Received in revised form 5 June 2026; Accepted 11 June 2026
Available online 16 June 2026

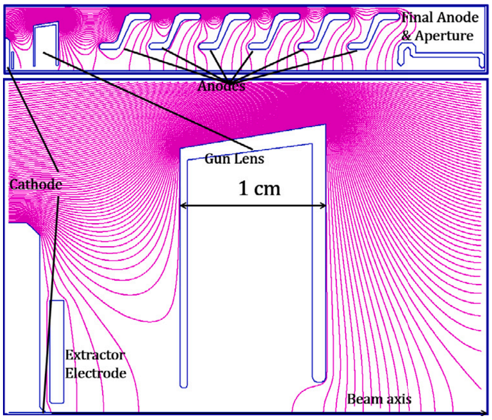

Fig. 1. Cross-section of the generic electrostatic gun column. Electrons are accelerated from the flat cathode by the strong field of the extractor electrode (A1), focused with the independently biased gun lens electrode (A2), and stepped to 200 keV by the accelerating stack. The final aperture serves as the output plane for quantifying beam properties.

In this work, we pursue source-level aberration suppression by reconfiguring the cathode–anode region as a combined accelerator–condenser system. This design builds on the long history of multi-electrode electrostatic source optics in electron microscopy, including tetrode-type guns and shaped-electrode geometries developed to control pre-accelerator focusing, virtual source position, aperture aberrations, and field gradients [19–22]. Building on this approach, we introduce an extractor pre-lens and tune the electrode voltages to keep the beam envelope small in regions of strong on-axis field curvature, thereby reducing the third-order contribution to C_s.

The present work should therefore not be viewed as a new electrode topology, but as a space-charge-aware reoptimization of this class of source optics for a different operating regime: a flat, laser-driven photocathode emitting nanosecond pulses at milliampere peak current. In this regime, the dominant design challenge is the coupling of space-charge-driven angular expansion into source-region spherical aberration, rather than the low-current optimization metrics usually emphasized for field-emission sources. Using an off-axis transfer-map model with Green's function aberration integrals, benchmarked against Superfish field calculation and GPT space-charge simulations, we show that C_s can be reduced from $\gtrsim 150$ mm to a few millimeters at 200 keV while sustaining peak currents near 1 mA. These results provide operating maps and design rules for next-generation DTEM sources optimized for high-brightness single-shot imaging.

2. 200 keV electrostatic DTEM source

Sharp tip field emission guns (FEGs) provide excellent beam quality in conventional or stroboscopic TEM modes, but they are unsuitable for the high peak currents required in single-shot DTEM. Tip emitters cannot withstand the current densities associated with nanosecond, milliampere pulses and would rapidly fail under such load [23]. In contrast, a flat photocathode in a modified FEG-type electrostatic gun provides robust operation at high charge, with controllable laser-driven photoemission and mitigation of space-charge effects with laser shaping. Compared to thermionic DTEM guns, this approach supports higher peak current, lower transverse emittance, and improved energy spread.

Single-shot DTEM requires at least 10^7 electrons per pulse to form a complete image. At 200 keV, this corresponds to nanosecond-scale bunches carrying peak currents on the order of milliamperes. In this regime, space-charge forces are significant but still amenable to analytic treatment, allowing rapid optimization of source brightness. Mitigation strategies rely on accelerating electrons quickly to minimize their time at low velocity and high density, which demands large extraction fields across the flat cathode. A FEG-type geometry with dedicated extractor and gun-lens electrodes enables independent tuning of these functions, allowing higher currents and improved spatial coherence compared to thermionic sources.

The baseline "generic gun" (GG) geometry used in this study is shown in Fig. 1. It consists of: (i) a flat photocathode with radius set to 150 μm biased at −200 kV, providing 200 keV kinetic energy at the exit; (ii) an extractor electrode (A1) held a few kilovolts above the cathode to establish the strong accelerating field needed to overcome space charge; (iii) a gun lens electrode (A2) with independent voltage control of 2–10 kV relative to the cathode, shaping the beam envelope and ideally focusing it through the final aperture; and (iv) a stack of anodes stepping the beam to ground potential over ∼20 cm, with the final aperture serving as the effective output plane. This configuration is representative of commercial electrostatic TEM guns, but is here treated generically to allow systematic exploration of operating points and design modifications.

In defining the GG, the A2 electrode was positioned within ∼1 cm of the cathode to maximize throughput, ensuring that beams over a range of initial angles (< 50 mrad) are accepted. In this study we keep the A2 position and aperture geometry fixed to represent a practical DTEM column, and focus our optimization on the extractor region. For each candidate extractor configuration we modify the conductors, regenerate the electrostatic field map (e.g. with Poisson), and analyze the resulting aberrations within the same transfer-map and GPT framework. This restricted design space is intentional. We do not attempt a global search over all diode, tetrode, shaped-electrode, or magnetic source configurations [24]. Instead, we consider modifications that preserve the basic architecture of a conventional electrostatic TEM gun column while adding enough freedom to decouple the cathode launch field from the early focusing strength. This choice allows the dominant physics of the DTEM regime to be isolated: the conversion of space-charge-driven angular spread into source-region spherical aberration. Alternative variants could be analyzed within the same framework and may yield further improvements, but they are outside the scope of the present benchmark study. In the same way, a more global optimization that also varies the A2 spacing and aperture sizes is left for future work. To evaluate and optimize each candidate geometry, we use the workflow summarized in Fig. 2. For each axisymmetric electrode geometry, the electrostatic potential is first calculated with Superfish. The resulting field maps are then used in two complementary ways. First, the on-axis potential and its derivatives are used in the transfer-map and Green's-function calculation to rapidly estimate the dominant third-order image errors. Second, the same field maps are imported into GPT for particle tracking with three-dimensional space-charge forces. The Green's-function model identifies the origin of the aberration and guides the voltage and geometry scans. The GPT simulations then provide the self-consistent benchmark for the selected operating points. Other charged-particle-optics methods could be used for the external-field aberration analysis, but the present workflow was chosen because it connects the conventional language of aberration coefficients to the high-current, flat-photocathode, space-charge-dominated source dynamics considered here.

Performance near the cathode is strongly influenced by the mean transverse energy (MTE), laser spot size, and accelerating field. For typical copper photocathodes with 0.1 eV < MTE < 1 eV, initiating photoemission with a ∼ 10 μm laser spot yields normalized emittances suitable for imaging applications [25,26]. In practice, the laser spot must also be kept tight because the cathode geometry is effectively a flattened tip. Increasing the illumination radius beyond ∼10 μm causes the beam to sample stronger fringing fields at the cathode edge, introducing additional geometric aberrations that dilute brightness. Thus, spot-size scaling is constrained not only by emittance considerations but also by electrode geometry.

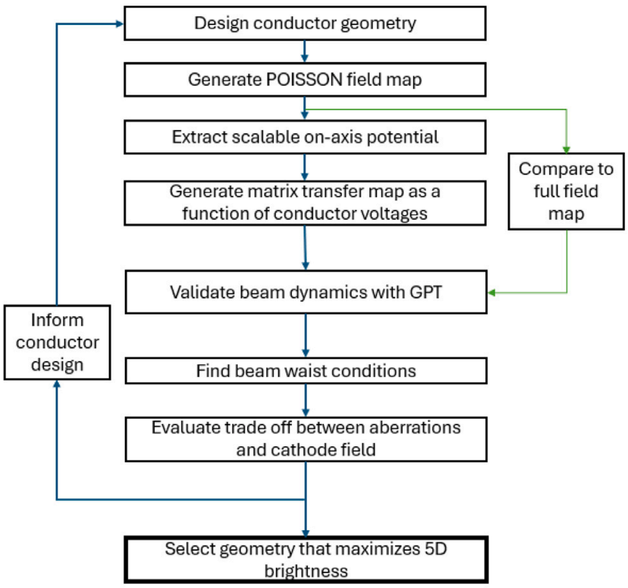

Fig. 2. Workflow for modeling and optimizing the 200 keV DTEM gun geometry. Analytical envelope and transfer-map models with space charge are benchmarked against SUPERFISH and GPT, and used to extract aberration coefficients via Green's-function integration.

Since the emission profile is a uniform disk, the cathode emittance is given by [27]:

$$\epsilon_{n,x} = \frac{R}{2}\sqrt{\frac{\mathrm{MTE}}{mc^2}}, \tag{1}$$

where R is the laser spot radius.

In the long-pulse, "cigar" regime relevant to nanosecond DTEM, the maximum current that can be launched is given by

$$I_{\mathrm{sat}} = \frac{\sqrt{2}}{9} I_a \left(\frac{eE_0R}{mc^2}\right)^{3/2}, \tag{2}$$

where $I_a = 17$ kA is the Alfvén current [7]. For example, with $E_0 = 10$ MV/m and $R = 10$ μm, the saturation current is about 7 mA. To remain in the regime where space-charge-induced emittance growth is negligible and brightness is preserved, we restrict our analysis to currents within a few mA so as to avoid virtual cathode instabilities. Explicitly, the brightness is the ratio of beam current to the product of the (equal in this case) normalized transverse emittances, $B = I/\epsilon_{n,x}^2$, so in this case a reasonable upper bound is $B \lesssim 2\times10^{13}$ A/m^2 (assuming 1 mA with 1 eV MTE).

Within this operating window, as more current is driven into the system, the normalized emittance of the generic gun remains essentially constant and equal to the thermal emittance for uniform illumination, while the transverse angular spread increases linearly with current. The latter behavior follows from the near saturating space-charge fields of Ref. [28], which — after scaling by I_0/I_{sat} and calculating the impulse on the transverse momentum (derived in Appendix A) — predict a current-induced angular contribution:

$$\Delta\sigma_{\theta,\mathrm{sc}} \approx \frac{\pi}{12\gamma\beta}\frac{I_0}{I_{\mathrm{sat}}}\sqrt{\frac{eE_0R}{mc^2}}. \tag{3}$$

In this expression, $\gamma\beta$ is the axial momentum at the reference plane. For uniform illumination the transverse space-charge field is linear in the transverse coordinate, and therefore introduces no emittance growth—only an additional correlated angular kick. This is illustrated in Fig. 3, wherein (a) compares the resulting theory curve with a GPT simulation

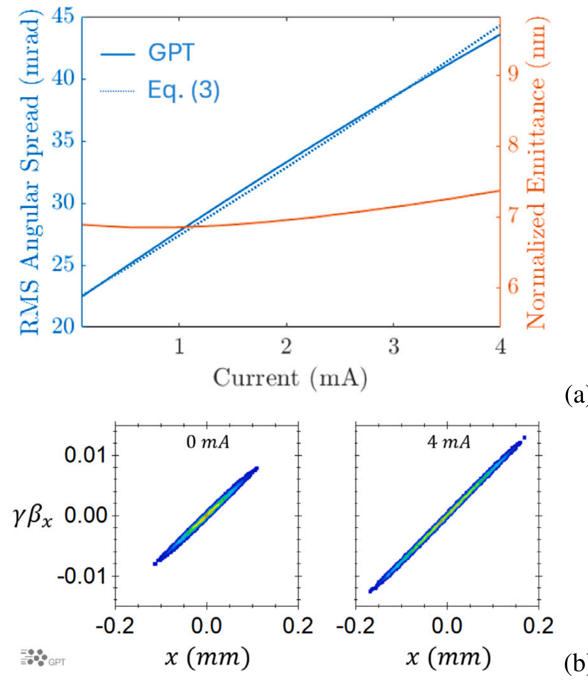

Fig. 3. (a) Rms angular spread and normalized emittance at a screen 1.25 mm from the cathode for the generic gun. The normalized emittance remains essentially constant, while the rms angular spread increases linearly with current due to collective space-charge forces. (b) A direct comparison of phase spaces without and with current.

of photoemission to a screen 1.25 mm downstream of the cathode. Fig. 3(b) shows how the space charge kick simply adds to the linear correlation. In other words, the phase profile in Fig. 3(b) is stretched linearly such that the phase space area is preserved. Injected into the gun lens, these larger angles sample stronger on-axis field curvature, producing third-order image errors dominated by spherical aberration and motivating the geometric modifications introduced in the next section.

3. Electrostatic transfer map with space charge and Green's function

To analyze how electrode voltages and geometry shape transport beyond the linear regime, we extend the transfer-map approach to third order while including the effects of space charge. Compared to historical literature, treatments of ray transfer in electrostatic or magnetic optics have focused on external fields alone, but here we incorporate self-fields perturbatively. In particular, we retain the curvature of the charge density, which is usually neglected but becomes important when the beam envelope is tightly confined, and the profile is non-uniform. This contribution generates cubic correlations in the phase space that are effectively indistinguishable from spherical aberration, similarly to what happens in the propagation from the sample to the detector [29]. By developing the third-order ray equation in this way, the formalism provides a direct analytic link between electrode geometry, operating voltages, and both geometric and collective aberrations, offering a compact framework to complement full three-dimensional particle tracking.

The preceding section established the phase-space conditions at a screen 1.25 mm downstream of the cathode, where the dependence of divergence on current was quantified using GPT. That distribution serves as the initial condition for the present analysis: rather than running full particle tracking for every voltage setting, we propagate this sample phase space through the column using the transfer-map formalism derived here. Starting from the relativistic equations of motion, the external potential is expanded off-axis and combined with the space-charge potential. Retaining terms to third order in the transverse coordinates introduces field-curvature contributions along with additional density-curvature and axial density terms. This approach enables rapid exploration of operating points and geometry modifications, with attractive conditions subsequently verified through full GPT simulations. We leave the details of the third-order derivation in the appendix, but will outline here the important steps that show how the linear transport map is obtained.

We start by expanding off axis a cylindrically symmetric externally applied potential as

$$\phi_{\rm ext}(r,z) = \sum_{n=0}^{\infty} (-1)^n \frac{V^{(2n)}(z)}{(n!)^2}\left(\frac{r}{2}\right)^{2n}, \tag{4}$$

where $V^{(2n)}(z) = \partial_r^{2n}\phi_{\rm ext}(0,z)$ are the even on-axis radial derivatives and $V^{(0)}(z) = V(z)$ [30]. To include third-order ray effects it suffices to retain terms through r^4.

The total potential will also include the contribution of the space charge i.e. $\phi = \phi_{\rm ext} + \phi_{\rm sc}$. The equations of motion depend on the space charge field $-\nabla\phi_{\rm sc}$. For a cylindrically symmetric long beam where the slice dependence is negligible (an infinite beam approximation), the charge density can be expanded in an even-powered Maclaurin series,

$$\rho(r;z) = \sum_{n=0}^{\infty} \frac{\rho^{(2n)}(z)}{(2n)!} r^{2n}, \tag{5}$$

from which applying Gauss' law we retrieve the radial field

$$E_r(r;z) = \frac{1}{\varepsilon_0 r}\int_0^r \rho(\xi;z)\,\xi\,d\xi = \frac{\rho^{(0)}(z)}{2\varepsilon_0} r + \frac{\rho^{(2)}(z)}{8\varepsilon_0} r^3 + \cdots. \tag{6}$$

For a Gaussian transverse profile, $\rho^{(0)} = I_0/(2\pi\sigma_x^2 c\beta)$ and $\rho^{(2)} = -I_0/(2\pi\sigma_x^4 c\beta)$ depend on the local rms envelope $\sigma_x(z)$ [29] and axial velocity β. In this context, γ and β refer to the design trajectory. Different distributions have the same dependence on σ_x but with different prefactors.

With the paraxial definition $x' = \beta_x/\beta_z \approx \beta_x/\beta$, linearizing (i.e. keeping only first-order terms in) the ray equation, one obtains

$$x'' + \frac{(\gamma\beta)'}{\gamma\beta} x' = \frac{e\,V''}{2mc^2\,\gamma\beta^2}\,x + \frac{K(z)}{\sigma_x^2}\,x, \tag{7}$$

where $K(z) = I_0/(I_a\gamma^3\beta^3)$ is the transverse perveance. Transforming to normalized coordinates $X = x/\sqrt{\tilde{p}}$ with $\tilde{p}(z) \equiv \gamma(z)\beta(z)$ removes the mixed term and gives Hill's equation $X'' + \kappa(z)X = 0$ where

$$\kappa(z) = \frac{\gamma^2+2}{(\gamma\beta)^4}\left(\frac{eV'}{2mc^2}\right)^2 + \frac{K(z)}{\sigma_x^2(z)}. \tag{8}$$

The corresponding rms envelope equation which is needed to calculate the evolution of σ_x in $\kappa(z)$ is [31]

$$\sigma_x'' + \frac{(\gamma\beta)'}{\gamma\beta}\sigma_x' + \frac{\varepsilon_{n,x}^2}{(\gamma\beta)^2\sigma_x^3} = \frac{e\,V''}{2mc^2\,\gamma\beta^2}\,\sigma_x + \frac{K(z)}{\sigma_x}. \tag{9}$$

We first solve the envelope equation, Eq. (9), to obtain $\sigma_x(z)$; this is then used in $\kappa(z)$ to solve the first-order ray equation, Eq. (7).

The linear transport can be expressed in terms of the two linearly independent solutions to Hill's equation, denoted C_x and S_x. These play the role of cosine- and sine-like functions for the focusing channel and allow the motion to be written in a compact matrix form. The general solution for initial (x_0, x_0') is then

$$\begin{pmatrix} x \\ x' \end{pmatrix}_s = \sqrt{\frac{\tilde{p}(s_0)}{\tilde{p}(s)}}\begin{pmatrix} 1 & 0 \\ -\frac{\tilde{p}'(s)}{\tilde{p}(s)} & 1 \end{pmatrix}\begin{pmatrix} C_x(s) & S_x(s) \\ C_x'(s) & S_x'(s) \end{pmatrix} \times \begin{pmatrix} 1 & 0 \\ \frac{\tilde{p}'(s_0)}{\tilde{p}(s_0)} & 1 \end{pmatrix}\begin{pmatrix} x_0 \\ x_0' \end{pmatrix} = \begin{pmatrix} R_{11}(s) & R_{12}(s) \\ R_{21}(s) & R_{22}(s) \end{pmatrix}\begin{pmatrix} x_0 \\ x_0' \end{pmatrix}. \tag{10}$$

This matrix form shows that the transport is governed by the functions C_x and S_x in the case of an evolving longitudinal momentum $p(s) = \gamma\beta$, all of which depend explicitly on the on-axis potential $V(z)$ [32]. In this way, the effect of electrode voltages enters directly through the potential profile, making it possible to evaluate transport properties without full particle tracking.

Finally, the Green's function constructed from the fundamental solutions C_x and S_x provides a compact way to evaluate higher-order deviations [33]. It is written as

$$\mathcal{G}_x(z,s) = \sqrt{\frac{\tilde{p}(z)}{\tilde{p}(s)}}\left[C_x(s)S_x(z) - S_x(s)C_x(z)\right], \tag{11}$$

so that the third-order displacement at position z is

$$\delta x(z) = \int_{z_0}^{z} f(x,y;s)\,\mathcal{G}_x(z,s)\,ds, \tag{12}$$

where $f(x,y;s)$ represents the driving term, such as the cubic space-charge force or the field-curvature contributions. In this form, all dependence on electrode settings enters through the on-axis potential and its derivatives, allowing efficient scans of voltages and geometries without rerunning full particle tracking.

This Green-function formalism is straightforward to implement in MATLAB, enabling rapid scans of operating points directly from the on-axis potential. In the next section we use the resulting third-order ray equation to identify the dominant contribution to the aberration coefficient, then apply the model to scan extractor and gun-lens voltages for different extractor conductor configurations, optimizing for minimal third-order deviations. In doing so, we benchmark the predicted third-order trajectory deviations against full GPT particle tracking, confirming the accuracy of the linear model while carrying out the optimization.

4. Geometry-driven aberration suppression

As established in Fig. 3, below saturation the normalized emittance of the generic gun remains nearly constant under uniform illumination, while the transverse divergence grows linearly with current. When injected into the gun lens, these larger launch angles sample strong curvature of the on-axis voltage profile $V''(z)$, converting divergence into third-order image errors. The dominant contribution, derived in Appendix B, arises from the correction to the $1/\gamma\beta^2$ for off-axis rays, which factor into Eq. (B.7) and couples large initial angles into cubic deviations of the trajectory. Retaining this term leads to the spherical aberration integral

$$\delta x(z) \simeq \frac{1}{8}\int_{z_0}^{z} \frac{\gamma^2+1}{(\gamma^2-1)^2}\left(\frac{eV''}{mc^2}\right)^2 x^3\,\mathcal{G}_x\,ds, \tag{13}$$

from which the spherical aberration coefficient C_s can be extracted as

$$C_s \simeq \frac{1}{8R_{11}(z)}\int_{z_0}^{z} \frac{\gamma^2+1}{(\gamma^2-1)^2}\left(\frac{eV''}{mc^2}\right)^2 R_{12}^3\,\mathcal{G}_x\,ds. \tag{14}$$

Other higher-order terms in Eq. (B.7) were found to be subdominant. Thus, this contribution to spherical aberration is the principal bottleneck to brightness preservation in the generic gun.

The severity of this effect scales in two ways: through the curvature of the on-axis field and through the transverse size of the beam in regions of high curvature. Large MTE or higher currents exacerbate both, as the beam expands more rapidly and samples stronger nonlinearities. Near the cathode the phase space remains nearly linear, but by the time the beam is focused to a waist by the A2 lens, cubic correlations have developed in the final phase space. These distortions trace directly back to spherical aberration driven by C_s growth in regions of strong field curvature. In practice, this means that even when collective effects are modest, geometric aberrations seeded by divergence dominate the emittance growth budget.

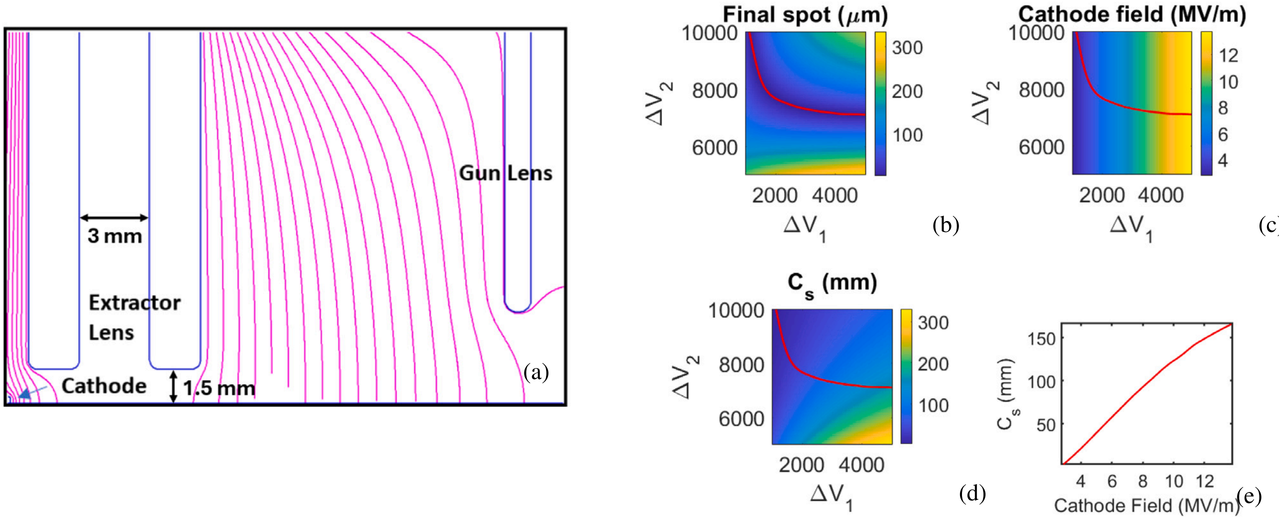

Fig. 4. (a) Coupled extractor-lens geometry: the added electrode enables prefocusing of the beam into the gun lens but its voltage remains tied to the extraction field. (b–e) Operating maps for this geometry: (b) final spot size, (c) cathode field, (d) spherical aberration C_s vs. extractor and gun-lens voltages (red contour: near-minimum-spot condition), and (e) trade-off between C_s and cathode field along that contour.

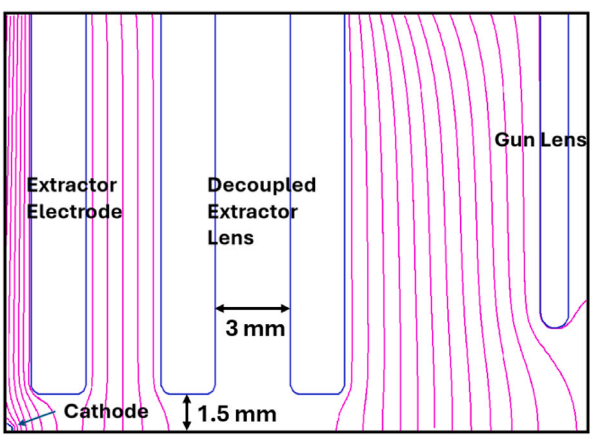

Fig. 5. Final iteration of the modified gun geometry with a high-field extractor electrode followed by a decoupled extractor lens. This configuration maintains a ~10 MV/m cathode field while retaining the same suppression of C_s by improving the collimation into the gun lens.

Chromatic and higher-order geometric aberrations were also estimated to determine whether they become limiting after suppression of the dominant third-order spherical term. For the operating points considered here, the modeled energy spread remains in the few-eV range at 200 keV, corresponding to a relative spread of order $\Delta E/E \sim 10^{-5}$. Even assuming a conservative 10 cm chromatic aberration coefficient C_c and an angular spread $\alpha \sim 10$ mrad, the estimated chromatic blur $\sigma_c \sim C_c \alpha \frac{\Delta E}{E}$, remains at the scale of tens of nanometers. This is small compared with the source-size and spherical-aberration-driven brightness degradation emphasized here. Similarly, the next term in the same expansion that produces Eq. (14) gives an estimated fifth-order coefficient of order $C_5 \sim 10^2$ mm. The associated fifth-order blur scales as $C_5\alpha^5$ and remains below the nanometer scale for $\alpha \sim 10$ mrad. These estimates indicate that, within the modeled operating range, chromatic blur and fifth-order geometric aberration are not the dominant limitations. The remaining source-level degradation is instead governed primarily by residual third-order spherical aberration and nonlinear transverse space-charge effects.

We also checked whether the tighter source-region confinement in the modified geometry significantly increases stochastic electron–electron energy broadening at 1 mA. Additional GPT simulations using the `spacecharge3Dtree` binary interaction model showed no appreciable binary-scattering-induced broadening over the first 10 mm of propagation, where the beam is slowest and densest. The total energy spread remained in the 3–5 eV range. At higher currents, the more important energy-spread mechanism is expected to be the correlated longitudinal chirp from collective space-charge fields, rather than stochastic binary scattering.

We therefore focus the geometry optimization on suppressing the dominant third-order spherical contribution while avoiding excessive beam compression that would enhance nonlinear space-charge aberrations. To this end, we first consider a modified geometry in which the extractor electrode is reshaped into an extractor lens, Fig. 4(a). In this coupled configuration, the added electrode prefocuses the beam into the gun lens, confining the envelope upstream so that the region of large $V''(z)$ is sampled less strongly and the effective spherical aberration is reduced. However, because the extractor lens voltage remains tied to the extraction field, reducing C_s by stronger prefocusing inevitably comes at the cost of lowering the cathode field.

The parameter space of extractor-lens and gun-lens voltages was scanned to quantify the trade-off between C_s and extraction field. Figs. 4(b–e) show the resulting maps of exit spot size, cathode field, and spherical aberration. The red contour traces operating points that minimize the final spot size. Along this contour, C_s decreases by more than an order of magnitude — from over 150 mm, close to the generic gun value, down to ~5 mm — while the cathode field decreases in parallel, as shown in Fig. 4(e). The coupled extractor lens therefore reshapes, rather than removes, the fundamental trade-off: optimal performance is achieved where the cathode field remains sufficient for emission yet C_s is suppressed, but the two cannot be varied independently.

To decouple the cathode field from the focusing strength that controls C_s, in the final design we use a high-field extractor electrode followed by an independent extractor lens, the geometry of which is shown in Fig. 5. This configuration maintains a ~10 MV/m cathode field for mA-level emission while independently adjusting the prefocusing into the gun lens to suppress C_s. In what follows, all "optimized"

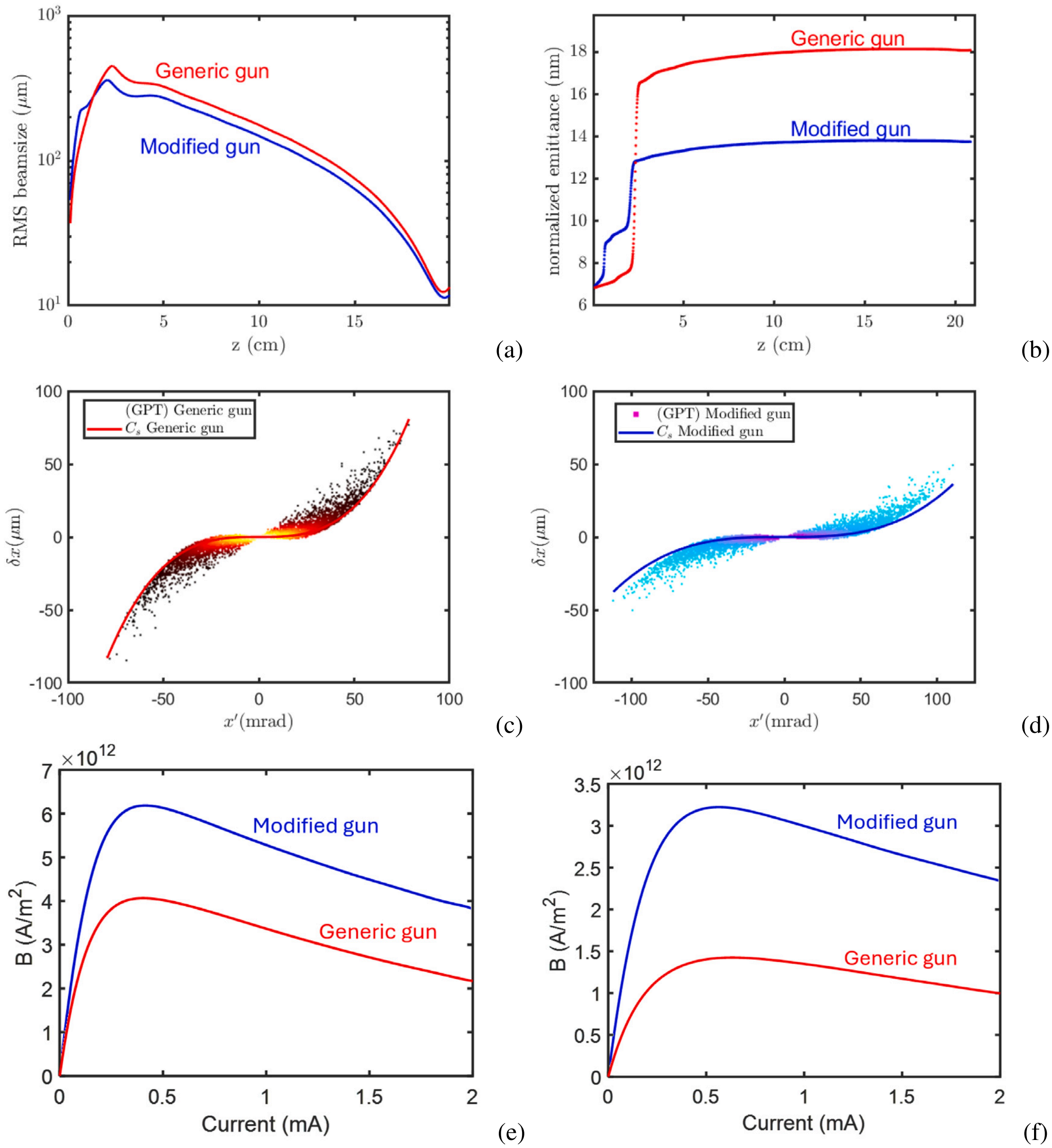

Fig. 6. Generic vs. modified gun at 1 eV MTE and 1 mA peak current. (a) Beam envelopes show reduced beam size in the modified configuration. (b) Normalized emittance growth is suppressed. (c–d) Cubic deviations at the aperture: GPT results (points) and Green's-function predictions (curves) show C_s reduced from ~150 mm to ~10 mm. Brightness as a function of current. (e) For MTE = 0.5 eV and (f) for MTE = 1 eV. The modified geometry improves peak brightness and extends the usable current range, particularly critical at higher MTE.

simulations use this decoupled-extractor configuration compared to the original generic gun.

Direct comparison between the generic and final modified geometry demonstrates the gain under matched initial conditions (10 μm cathode spot, MTE = 1 eV, 1 mA peak current). As shown in Fig. 6(a), the modified gun confines the beam envelope more tightly. The corresponding emittance evolution in Fig. 6(b) shows that this confinement suppresses emittance growth relative to the generic case. Figs. 6(c) and (d) show the cubic deviations from the linear correlation in the phase space that cause the emittance growth at a plane just upstream of the final aperture. Panel (c) corresponds to the generic gun, while panel (d) shows the modified geometry, for which the cubic spherical correlations are reduced. In both panels, the C_s predicted by Eq. (14) is overlaid on the deviations extracted from the GPT simulations, decreasing from $\sim$ 150 mm for the generic gun to $\sim$ 10 mm for the modified geometry, in good agreement with the Green's-function model.

A key subtlety is that shrinking the envelope eventually strengthens collective nonlinearities. In the third-order equation of motion, Eq. (B.7), this appears in the term proportional to the second transverse derivative of the charge density, $\rho^{(2)}$. Even with a uniform emission profile, the projected transverse density becomes approximately Gaussian through most of the column because the launch angles are Gaussian; thus $\rho^{(2)} \neq 0$ and the corresponding term's magnitude grows with local compression. As the extractor and electrodes are tuned to keep the envelope small in regions of strong field curvature, the increased on-axis density enhances the $\rho^{(2)}$ term, exacerbating cubic correlations. This space-charge contribution, discussed in Ref. [29] in the context of post sample optics, therefore sets a practical upper bound: beyond a point, further geometric suppression of C_s is offset by $\rho^{(2)}$-driven aberration.

A simple estimate of this crossover is obtained by comparing the emittance and perveance terms in the envelope equation. For a normalized emittance of 10 nm and a 1 mA beam current at 200 keV, the nonlinear space-charge contribution is expected to become appreciable when the beam size in the lens region is reduced to below 40 μm. The optimized cases studied here keep the beam size larger than this scale, so the dominant benefit remains the reduction of launch-angle-driven spherical aberration. We therefore did not pursue stronger focusing, since it would increase on-axis density and eventually trade one aberration mechanism for another.

The improvement in usable brightness is summarized in Fig. 6(e–f). For a modest MTE of 0.5 eV, Fig. 6(e) shows that the modified geometry increases the brightness by $\sim 40\%$ above the generic gun across the current range. At higher MTE (1 eV), Fig. 6(f) shows that, over the same range, the modified geometry sustains performance to ∼2 mA with a little more than a $\sim 100\%$ increase in usable brightness. Thus, extractor-lens prefocusing benefits not only ideal photocathodes but also mitigates the cascading degradation associated with less favorable emission conditions.

Several practical implementation issues should be noted. The present calculations are axisymmetric and therefore establish the on-axis design principle rather than a full mechanical tolerance budget. Small transverse offsets or tilts of the extractor assembly would not change the cylindrically symmetric spherical aberration coefficient C_s extracted from the on-axis model, but would break axial symmetry and introduce steering, coma-like distortions, and other higher-order geometric aberrations. GPT simulations indicate that transverse centroid offsets of approximately 20 μm produce less than 10% emittance growth while retaining roughly 80–90% of the nominal brightness, suggesting that the envelope-confinement mechanism remains robust to modest transverse misalignments. Likewise, a spherical-aberration analysis in which relative tilts between the extractor and gun lens are represented as a shift in the mean emission angle suggests tolerances on the order of 10–20 mrad for comparable emittance growth and brightness degradation. Larger transverse offsets approaching the edge of the cathode good-field region ($R_{cathode}/2 \approx 50$ μm), or correspondingly larger angular misalignments, produce substantially greater emittance growth and brightness degradation. A dedicated tolerance study including all higher-order aberrations is therefore required before engineering implementation.

The modified geometry also does not require unusually large adjacent-electrode fields outside the cathode extraction region. While the cathode is intentionally operated at extraction fields of approximately 10 MV/m, the largest field between neighboring source electrodes in the optimized configuration is produced by a potential difference of approximately 3.5 kV across a minimum gap of about 0.75 mm, corresponding to a macroscopic field below 5 MV/m. These field levels are well within the range routinely employed in conditioned ultra-high-vacuum electron-optical systems, although local field enhancement from surface roughness, contamination, or sharp geometric features must still be controlled in a practical implementation.

5. Conclusion

We have investigated how electrostatic gun design determines the usable brightness of 200 keV DTEM sources at the milliampere peak-current level. Using an off-axis transfer-map model with Green's-function aberration integration, benchmarked against Poisson/Superfish and GPT, we quantified how space-charge-induced divergence in conventional guns seeds strong spherical aberration. By reshaping the cathode–anode assembly to act simultaneously as an accelerator and a condenser lens, and by co-tuning the extractor-lens and gun-lens voltages, the spherical aberration coefficient C_s is reduced from more than 150 mm to ∼5–10 mm while maintaining fields sufficient for mA-level emission. This establishes geometry-driven suppression of C_s as a viable route to brightness preservation.

An important implication is that this method is not limited to a single electrode modification but defines a framework for systematic source optimization. The transfer-map and Green's-function formalism provides rapid evaluation of higher-order image errors directly from on-axis fields, enabling efficient exploration of geometry space. In principle, this approach can be wrapped into an automated loop that iterates over electrode positions, gaps, and apertures, with Poisson/Superfish supplying the field maps and GPT validating the final transport. Such integration would allow convergence toward globally optimal designs rather than one-off improvements, bridging analytic design rules with full 3D particle tracking.

At the system level, lowering intrinsic C_s at the source also reduces the post-specimen current required to achieve a given dose, mitigating projection-column space-charge aberrations and preserving image fidelity in single-shot DTEM. Along the minimum-spot operating contour, the present design achieves sub-10 μm waists at the exit aperture for MTE = 0.1–1 eV and ∼1 mA peak current, conditions that correspond to brightness levels suitable for next-generation ultrafast electron microscopy.

Although 200 keV is used here as the benchmark energy, the same source-region design principle should remain relevant at other terminal voltages, provided the electrode settings are retuned. The reason is that the dominant effect of the modified geometry occurs near the cathode, where the decoupled extractor allows the launch field and early focusing strength to be adjusted so as to reduce the coupling of space-charge-driven angular spread into spherical aberration. If the near-cathode field configuration and early beam acceleration are kept comparable, this mechanism should persist qualitatively at other operating energies. The balance of limitations, however, changes with energy. For fixed normalized emittance, the geometric emittance scales as $1/\beta\gamma$, while the generalized perveance scales approximately as $1/\beta^3\gamma^3$. Lower-voltage operation, such as 80 keV, is therefore more sensitive to space charge and chromatic blur for a given current and absolute energy spread while higher-voltage operation is more forgiving. Thus, the present geometry should be viewed as a 200 keV benchmark and not as a universal optimum across all DTEM operating voltages.

These results demonstrate that geometry-driven aberration suppression, combined with an iterative design framework, offers a direct and general pathway to high-brightness, low-aberration DTEM sources.

CRediT authorship contribution statement

Paul Denham: Writing – original draft, Visualization, Validation, Software, Investigation, Formal analysis, Data curation, Conceptualization. **Pietro Musumeci:** Writing – original draft, Supervision, Investigation, Conceptualization. **Daniel J. Masiel:** Supervision, Methodology, Conceptualization. **Bryan W. Reed:** Writing – original draft, Supervision, Software, Methodology, Investigation, Conceptualization.

Declaration of competing interest

The authors declare the following financial interests/personal relationships which may be considered as potential competing interests: Paul Denham reports financial support was provided by STROBE. Bryan W. Reed reports a relationship with Integrated Dynamic Electron Solutions (IDES, Inc.) that includes: employment. Daniel J. Masiel reports a relationship with Integrated Dynamic Electron Solutions (IDES, Inc.) that includes: employment. If there are other authors, they declare that they have no known competing financial interests or personal relationships that could have appeared to influence the work reported in this paper.

Acknowledgments

P.D. acknowledges support from the National Science Foundation STROBE Science and Technology Center under Grant No. DMR-1548924.

Appendix A. Derivation of space-charge-induced rms angular spread

We define the normalized longitudinal variable $\xi = z/R$, then in the cathode vicinity, the space–charge field for a cigar pulse with uniformly illuminated transverse spot is given by [28]:

$$E_z^{\rm sc} \approx \frac{\frac{I_0}{I_{\rm sat}}E_0}{\left(1+0.6\,\xi^{1/3}+2.5\,\xi\right)^2}, \tag{A.1}$$

$$E_x^{\rm sc} \approx \frac{I_0}{I_{\rm sat}}\frac{E_0}{3}\frac{x}{R}\frac{\xi}{1+\xi^2} \tag{A.2}$$

Over the short region where the transverse kick is largest, the axial acceleration can be taken as due to the applied field alone, so the nonrelativistic speed is

$$v(\xi) = \sqrt{\frac{2eE_0R\,\xi}{m}}. \tag{A.3}$$

The transverse impulse is

$$\begin{aligned}\Delta p_x &= \int eE_x^{\rm sc}\,dt = \int_0^\infty eE_x^{\rm sc}\,\frac{dz}{v}\\ &= x_0\frac{I_0}{I_{\rm sat}}\frac{eE_0}{3}\int_0^\infty \frac{\xi}{1+\xi^2}\frac{d\xi}{v(\xi)}\\ &= \frac{x_0}{R}\frac{I_0}{I_{\rm sat}}\frac{\pi}{6}\sqrt{meE_0R}.\end{aligned} \tag{A.4}$$

Hence, the angular kick (using $x' = p_x/\gamma mc\beta$) is

$$\Delta x'(x_0) = \frac{x_0}{R}\frac{\pi}{6\gamma\beta}\frac{I_0}{I_{\rm sat}}\sqrt{\frac{eE_0R}{mc^2}}\,. \tag{A.5}$$

For a uniform disk, the RMS beamsize is $\sigma_x = \sqrt{\langle x_0^2\rangle} = R/2$, so the increase in RMS angular spread is

$$\Delta\sigma_{\theta,\rm sc} = \frac{\pi}{12\gamma\beta}\frac{I_0}{I_{\rm sat}}\sqrt{\frac{eE_0R}{mc^2}}. \tag{A.6}$$

We find that including $E_z^{\rm sc}$ in the impulse calculation, which must be done numerically, is a very small, negligible correction because only the applied field is appreciable where the transverse impulse is localized.

Appendix B. Derivation of third-order ray equation

The equations of motion are obtained from the relativistic force equation $\frac{d\mathbf{p}}{dt} = -e\nabla\phi$, where e is the electron charge, m its mass, and $\mathbf{p} = mc\gamma\vec{\beta}$, with $\vec{\beta}$ the velocity vector normalized by c and $\gamma = 1/\sqrt{1-\beta^2}$. The longitudinal and transverse equations of motion are given by:

$$\begin{aligned}(\gamma\beta_z)' &= -\frac{e}{mc^2\beta_z}\frac{\partial\phi}{\partial z},\\ x'' &= \frac{e}{mc^2\gamma\beta_z^2}\left(\frac{\partial\phi}{\partial z}x' - \frac{\partial\phi}{\partial x}\right),\end{aligned} \tag{B.1}$$

where the prime indicates a derivative with respect to z.

The transverse equation can also be expressed in terms of the total velocity and Lorentz factor using $\beta^2 = \beta_z^2(1+x'^2+y'^2)$. After substituting, one obtains:

$$x'' = \frac{e}{mc^2\gamma\beta^2}(1+x'^2+y'^2)\left(\frac{\partial\phi}{\partial z}x' - \frac{\partial\phi}{\partial x}\right). \tag{B.2}$$

Energy conservation provides, at any given position,

$$\gamma(r,z) = \gamma_0 - \frac{e\phi(r,z)}{mc^2}. \tag{B.3}$$

γ and β for the design trajectory are expressed as:

$$\gamma_c(z) = \gamma_0 - \frac{eV(z)}{mc^2}, \quad \beta_c = \sqrt{1-1/\gamma_c^2}, \tag{B.4}$$

Expanding the factor $1/\gamma\beta^2$ for an arbitrary ray to second order in r about the design trajectory yields:

$$\frac{1}{\gamma\beta^2} = \frac{1}{\gamma_c\beta_c^2}\left(1 - \frac{e}{8mc^2}\frac{\gamma_c^2+1}{\gamma_c(\gamma_c^2-1)}V''(z)r^2+\cdots\right). \tag{B.5}$$

Upon substituting Eq. (B.5) into Eq. (B.2) one obtains the following:

$$\begin{aligned}x'' &= \frac{e}{mc^2\gamma_c\beta_c^2}\left(1 - \frac{e}{8mc^2}\frac{\gamma_c^2+1}{\gamma_c(\gamma_c^2-1)}(x^2+y^2)V''\right)\\ &\quad\times\left(1+x'^2+y'^2\right)\left(\frac{\partial\phi}{\partial z}x' - \frac{\partial\phi}{\partial x}\right).\end{aligned} \tag{B.6}$$

Including Eq. (6) with the applied potential expanded to third-order, we obtain the third-order ray equation:

$$\begin{aligned}x'' + \frac{(\gamma_c\beta_c)'}{\gamma_c\beta_c}x' &= \left(\frac{eV''}{2\,mc^2\gamma_c\beta_c^2} + \frac{e\rho^{(0)}}{2\epsilon_0 mc^2\gamma_c^3\beta_c^2}\right)x\\ &\quad - \frac{e\rho^{(2)}}{8\epsilon_0 mc^2\gamma_c^3\beta_c^2}r^3\\ &\quad - \left(\frac{e}{mc}\right)^2\left(\frac{\gamma_c^2+1}{8(\gamma_c^2-1)^2}\right)r^2\left(2V'V''x' + (V'')^2x + \frac{V''\rho^{(0)}}{\epsilon_0\gamma_c^2}x\right).\end{aligned} \tag{B.7}$$

Data availability

Data will be made available on request.

References

[1] A.H. Zewail, 4D ultrafast electron diffraction, crystallography, and microscopy, Annu. Rev. Phys. Chem. 57 (1) (2006) 65–103, http://dx.doi.org/10.1146/annurev.physchem.57.032905.104748.

[2] J.R. Dwyer, C.T. Hebeisen, R. Ernstorfer, M. Harb, V.B. Deyirmenjian, R.E. Jordan, R.J.D. Miller, Femtosecond electron diffraction: making the molecular movie, Philos. Trans. R. Soc. A: Math. Phys. Eng. Sci. 364 (1840) (2006) 741–778, http://dx.doi.org/10.1098/rsta.2005.1735.

[3] W.E. King, G.H. Campbell, A. Frank, B. Reed, J.F. Schmerge, B.J. Siwick, B.C. Stuart, P.M. Weber, Ultrafast electron microscopy in materials science, biology, and chemistry, J. Appl. Phys. 97 (11) (2005) 111101, http://dx.doi.org/10.1063/1.1927699.

[4] B.J. Siwick, J.R. Dwyer, R.E. Jordan, R.J.D. Miller, Ultrafast electron optics: Propagation dynamics of femtosecond electron packets, J. Appl. Phys. 92 (3) (2002) 1643–1648, http://dx.doi.org/10.1063/1.1487437.

[5] B. Barwick, D.J. Flannigan, A.H. Zewail, Photon-induced near-field electron microscopy, Nature 462 (2009) 902–906, http://dx.doi.org/10.1038/nature08662.

[6] I.V. Bazarov, B.M. Dunham, C.K. Sinclair, Maximum achievable beam brightness from photoinjectors, Phys. Rev. Lett. 102 (2009) 104801, http://dx.doi.org/10.1103/PhysRevLett.102.104801, URL https://link.aps.org/doi/10.1103/PhysRevLett.102.104801.

[7] D. Filippetto, P. Musumeci, M. Zolotorev, G. Stupakov, Maximum current density and beam brightness achievable by laser-driven electron sources, Phys. Rev. ST Accel. Beams 17 (2014) 024201, http://dx.doi.org/10.1103/PhysRevSTAB.17.024201, URL https://link.aps.org/doi/10.1103/PhysRevSTAB.17.024201.

[8] P. Denham, D. Garcia, A. Kulkarni, B. Schaap, Z. Liu, P. Musumeci, D. Filippetto, Experimental verification of space-charge saturation scaling laws in high-gradient photocathode RF guns, 2025, URL https://arxiv.org/abs/2511.02035 arXiv:2511.02035.

[9] L. Reimer, H. Kohl, Transmission Electron Microscopy: Physics of Image Formation, fifth ed., Springer, New York, 2008.

[10] D.B. Williams, C.B. Carter, Transmission Electron Microscopy: A Textbook for Materials Science, second ed., Springer, New York, 2009, http://dx.doi.org/10.1007/978-0-387-76501-3.

[11] T. LaGrange, G.H. Campbell, B.W. Reed, M. Taheri, J.B. Pesavento, J.S. Kim, N.D. Browning, Single-shot dynamic transmission electron microscopy for materials science, Appl. Phys. Lett. 89 (2006) 044105, http://dx.doi.org/10.1063/1.2236263.

[12] M.R. Armstrong, K. Boyden, N.D. Browning, G.H. Campbell, J.D. Colvin, W.J. DeHope, A.M. Frank, D.J. Gibson, F. Hartemann, J.S. Kim, W.E. King, T. LaGrange, B.J. Pyke, B.W. Reed, R.M. Shuttlesworth, B.C. Stuart, B.R. Torralva, Practical considerations for high spatial and temporal resolution dynamic transmission electron microscopy, Ultramicroscopy 107 (4–5) (2007) 356–367, http://dx.doi.org/10.1016/j.ultramic.2006.09.005.

[13] T. LaGrange, G.H. Campbell, B.W. Reed, M. Taheri, J.B. Pesavento, J.S. Kim, N.D. Browning, Nanosecond time-resolved investigations using the in situ dynamic transmission electron microscope (DTEM), Ultramicroscopy 108 (11) (2008) 1441–1449, http://dx.doi.org/10.1016/j.ultramic.2008.03.013.

[14] J.S. Kim, T. LaGrange, B.W. Reed, M.L. Taheri, M.R. Armstrong, W.E. King, N.D. Browning, G.H. Campbell, Imaging of transient structures using nanosecond in situ TEM, Science 321 (5895) (2008) 1472–1475, http://dx.doi.org/10.1126/science.1161517.

[15] B.W. Reed, T. LaGrange, R.M. Shuttlesworth, D.J. Gibson, G.H. Campbell, N.D. Browning, Solving the accelerator–condenser coupling problem in a nanosecond dynamic transmission electron microscope, Rev. Sci. Instrum. 81 (5) (2010) 053706, http://dx.doi.org/10.1063/1.3427234.

[16] D.H. Dowell, J.F. Schmerge, Quantum efficiency and thermal emittance of metal photocathodes, Phys. Rev. Spec. Top. - Accel. Beams 12 (2010) 074201, http://dx.doi.org/10.1103/PhysRevSTAB.12.074201.

[17] M. Haider, S. Uhlemann, E. Schwan, H. Rose, B. Kabius, K. Urban, Electron microscopy image enhanced, Nature 392 (6678) (1998) 768–769, http://dx.doi.org/10.1038/33823.

[18] O.L. Krivanek, N. Dellby, A.R. Lupini, Towards sub-aa electron beams, Ultramicroscopy 78 (1–4) (1999) 1–11, http://dx.doi.org/10.1016/S0304-3991(99)00013-3.

[19] W. Butler, Unpublished, in: Proceedings of the 6th International Congress for Electron Microscopy, Kyoto, 1966.

[20] K. Kuroda, T. Suzuki, Analysis of accelerating lens system in field-emission scanning electron microscope, J. Appl. Phys. 45 (3) (1974) 1436–1441.

[21] M. Denizart, S. Roques, F. Sonier, B. Jouffrey, J. Trinquier, Triode and tetrode guns for field emission electron microscopes, Ultramicroscopy 7 (1) (1981) 65–80.

[22] A. Crewe, D. Eggenberger, J. Wall, L. Welter, Electron gun using a field emission source, Rev. Sci. Instrum. 39 (4) (1968) 576–583.

[23] A. Feist, N. Bach, N. Rubiano da Silva, T. Danz, M. Möller, K.E. Priebe, T. Domröse, J.G. Gatzmann, S. Rost, J. Schauss, S. Strauch, R. Bormann, M. Sivis, S. Schäfer, C. Ropers, Ultrafast transmission electron microscopy using a laser-driven field emitter: Femtosecond resolution with a high coherence electron beam, Ultramicroscopy (ISSN: 0304-3991) 176 (2017) 63–73, http://dx.doi.org/10.1016/j.ultramic.2016.12.005, 70th Birthday of Robert Sinclair and 65th Birthday of Nestor J. Zaluzec PICO 2017– Fourth Conference on Frontiers of Aberration Corrected Electron Microscopy. URL https://www.sciencedirect.com/science/article/pii/S0304399116303709.

[24] M. Troyon, Magnetic field emission gun with zirconiated emitter: Performances at low voltage, Ultramicroscopy 28 (1–4) (1989) 98–102.

[25] P. Musumeci, et al., Advances in bright electron sources, Nucl. Instruments Methods Phys. Res. Sect. A: Accel. Spectrometers, Detect. Assoc. Equip. 907 (2022) 209–220, http://dx.doi.org/10.1016/j.nima.2018.03.019.

[26] R. Li, P. Musumeci, Single-shot MeV transmission electron microscopy with picosecond temporal resolution, Phys. Rev. Appl. 2 (2) (2014) 024003.

[27] D.H. Dowell, J.F. Schmerge, Quantum efficiency and thermal emittance of metal photocathodes, Phys. Rev. ST Accel. Beams 12 (2009) 074201, http://dx.doi.org/10.1103/PhysRevSTAB.12.074201, URL https://link.aps.org/doi/10.1103/PhysRevSTAB.12.074201.

[28] G. Shamuilov, A. Mak, K. Pepitone, V. Goryashko, Child-langmuir law for photoinjectors, Appl. Phys. Lett. (ISSN: 0003-6951) 113 (20) (2018) 204103, http://dx.doi.org/10.1063/1.5063888, arXiv:https://pubs.aip.org/aip/apl/article-pdf/doi/10.1063/1.5063888/14520529/204103_1_online.pdf.

[29] P. Denham, P. Musumeci, Space-charge aberrations in single-shot time-resolved transmission electron microscopy, Phys. Rev. Appl. 15 (2021) 024050, http://dx.doi.org/10.1103/PhysRevApplied.15.024050.

[30] F. Hinterberger, Ion optics with electrostatic lenses, 2006, http://dx.doi.org/10.5170/CERN-2006-012.27, URL https://cds.cern.ch/record/1005034.

[31] J.D. Lawson, The physics of charged-particle beams, second ed., in: International Series of Monographs on Physics, vol. 75, Oxford University Press, Oxford, England, 1988.

[32] C. Gulliford, I. Bazarov, New method for generating linear transfer matrices through combined rf and solenoid fields, Phys. Rev. ST Accel. Beams 15 (2012) 024002, http://dx.doi.org/10.1103/PhysRevSTAB.15.024002, URL https://link.aps.org/doi/10.1103/PhysRevSTAB.15.024002.

[33] H. Wiedemann, Particle Accelerator Physics, Springer Nature, 2015, URL https://link.springer.com/book/10.1007/978-3-319-18317-6.